Iridescence Reveals the Formation and Growth of Ice Aerosols in Martian Noctilucent Clouds

M.T. Lemmon [1], A. Vicente-Retortillo [2], S.D. Guzewich [3], M. de la Torre Juárez [4], A.C. Innanen [5], C.L. Campbell [5,6,7], J.N. Maki [4], M.C. Malin [8], and J.E. Moores [5]

[1] Space Science Institute, Boulder, CO, USA.

[2] Centro de Astrobiología (CAB), CSIC-INTA, Torrejón de Ardoz, Spain.

[3] NASA Goddard Space Flight Center, Greenbelt, MD, USA.

[4] Jet Propulsion Laboratory, California Institute of Technology, Pasadena, CA, USA

[5] York University, Toronto, ON, M3J1P3, Canada

[6] NASA Goddard Space Flight Centre, Greenbelt, MD, 20771, USA

[7] Catholic University of America, Washington DC, 20064, USA

[8] Malin Space Science Systems, San Diego, CA, USA

Corresponding author: Mark Lemmon (MLemmon@SpaceScience.org)

Key Points:

- Curiosity rover images reveal a previously unknown, visually spectacular cloud season in the Martian tropics during early southern autumn
- Iridescence in the noctilucent clouds requires a narrow particle size distribution, implying a brief evolution in a uniform environment
- Such images, with contextual information, probe the formation and growth processes within Martian clouds

Abstract

Water and carbon dioxide each form mesospheric clouds on Mars. At such altitudes (40-100 km), clouds may remain sunlit for part of the night. We describe a previously unreported, visually spectacular season of iridescent, noctilucent clouds visible in early southern autumn from the Curiosity rover's site in Gale crater. Ice nucleation begins near sunset with a narrow range of particle sizes, and the ice aerosols grow and precipitate. The iridescence, visible through three-color imaging, arises from locally uniform particle sizes resulting from similar growth histories. Colorful fall streaks show the clouds evolving, and a scattering corona shows size uniformity over large areas. The terminator was observed on the clouds, allowing the determination of cloud altitudes and a likely CO_2 composition. This is the first observation of particle size variations within individual Martian clouds, allowing a new probe of Martian cloud physics.

Plain Language Summary

Water and carbon dioxide each form high-altitude (40-100 km) clouds on Mars. Clouds at those altitudes on Earth can be noctilucent—night-shining—when they are illuminated by sunlight while the world below is dark. Noctilucent clouds have been seen on Mars but were not expected around the Curiosity rover site. Curiosity rover images from early southern autumn show clouds that are not only noctilucent, but they are also colorful with a mother-of-pearl appearance due to iridescence—such clouds are called *nacreous* on Earth. Curiosity's environmental data record shows that the clouds have consistently formed near sunset in that season. By looking at the timing of when Mars' shadow falls on the cirrus-like clouds, we found that they are 50-80 km high and are probably carbon dioxide ice, but there are lower layers of wave-like clouds that may be water ice. The pastel red, orange, green, and blue fringes of the clouds, which would be easily visible to an astronaut on Mars, help us understand the size of the cloud particles and how they grow and change.

1 Introduction

Mars has two atmospheric constituents that produce ice clouds, CO_2 and H_2O. The dominant gas, CO_2 forms clouds when thermal tides and gravity waves reduce already low temperatures below the CO_2 freezing point (Montmessin et al., 2007; Stevens et al., 2017; Jiang et al., 2019; Liuzzi et al., 2021). H_2O clouds typically form at 17-45 km (Smith et al., 2013) but can be found up to 85 km (Vincendon et al., 2011; Sánchez-Lavega et al., 2018). The seasonal behavior of both types of clouds has been mapped (Määtanen et al., 2010; Sefton-Nash et al., 2013; Clancy et al., 2019; Wolff et al., 2019; Slipsky et al., 2024). Diurnal sampling has been poor because satellites with sun-synchronous orbits sample only two times, and others sparsely sample diurnal, seasonal, and interannual variability (Aoki et al., 2018; Szantai et al., 2021), but there has been progress in daytime sampling (Atwood et al., 2022).

High-altitude clouds can be noctilucent, shining due to solar illumination when it is dark below, thus enhancing the visibility of optically thin clouds. Terrestrial noctilucent clouds comprise mesospheric water ice (Ostdiek & Thomas, 1993). Nacreous, or mother-of-pearl, clouds are (terrestrial) stratospheric water-ice clouds that are colorful due to iridescence caused by diffraction from a narrow distribution of cloud particle sizes (Reichardt et al., 2015). Color imaging of iridescence within noctilucent clouds can provide information about the size and evolution of the cloud particles (Sassen, 1979; Reichardt et al., 2015; Lange et al., 2022).

Noctilucent clouds have been observed on Mars from the surface and orbit (Smith et al., 1997; Connour et al., 2020; Hernández-Bernal et al., 2021; Toledo et al., 2023), and spectral interference effects that suggest iridescence have been reported in daytime CO_2 clouds (Clancy et al., 2019).

InSight detected noctilucent clouds at solar longitude (L_S) 16° in Mars Year (MY) 35 (25-04-2019; Banfield et al., 2020). Given InSight's location 600 km north of Curiosity, such >50-km altitude clouds were plausibly visible from Curiosity's Gale-crater location (137°E, 5°S). Before this, there were few reports of mesospheric clouds around Gale crater in early southern autumn. Such clouds were not expected due to the influence of Martian topography on tides, which suppresses gravity wave propagation to the mesosphere except around 0° and 270°E longitudes (Spiga et al., 2012). Aoki et al. (2018) reported an L_S=20-30° peak in afternoon mesospheric CO_2 clouds near 0° longitude with moderate optical depths that would be visible in the daytime. While the Opportunity rover imaged daytime cirrus clouds in that region in the same season (Lemmon et al., 2015), Curiosity has not seen similar clouds. Hernandez-Bernal et al. (2021) reported on twilight clouds at midlatitudes and not around the Curiosity site.

Using Curiosity data, we report the first images of nacreous clouds on Mars and use a long-term photometry record to show that the noctilucent cloud season was typical. Section 2 describes the observations of iridescence. Section 3 describes the environmental context for the clouds. Section 4 discusses the constraints on cloud characteristics and the window into cloud physics such data provides. Section 5 summarizes our conclusions.

2 Iridescence

2.1 Mastcam Images and Image Processing

Mastcam is Curiosity's color and multispectral stereo camera (Malin et al., 2019). Color images were obtained with a short-pass filter in series with Bayer-pattern microfilters (639±44, 553±38, and 494±38 nm for red, green, and blue) on the pixels (Bell et al., 2019). Due to the wider field of view (FOV) of the 34-mm focal length left eye, we used it for cloud imaging. The FOV, as commanded, was 16.6×14.8° and was sampled by 1328×1184 pixels with projected sizes of 74 µrad. Images were calibrated to radiance and *I*/*F* (radiance, or intensity, normalized to solar flux) using solar fluxes for each bandpass (Bell et al., 2019; Lemmon et al., 2022).

We used panoramic imaging to see clouds across the sky, emphasizing the sunset azimuth. Over mission sols 2422-2448 (2019-05-30 to 2019-06-26, L_S=33-45°), two imaging strategies were used. One used 23 images to obtain a 360° mosaic (23×1) covering ~13-27° elevation; the other used a westerly 3×2 mosaic, repeated to show motion (3×2×2). A second campaign over sols 3047-3091 (2021-03-03 to 2021-04-17, L_S=12-33°) included the 23×1 and 3×2×2 images as well as a small number of other mosaics. Panoramic images were processed into cylindrical mosaics using geometric information in image headers. The Sun was <-5.7° elevation for the observations reported here, meaning the sunlit clouds were noctilucent and above ~40 km altitude (looking west, 20° above the horizon).

All images were inspected in several color modes, including a linear I/F stretch, a gamma-corrected approximate true color stretch, and a normalized, chromaticity-like image (see Supporting Information Fig. S1). Chromaticity, which represents color information after the removal of intensity, is useful for objective studies of the color of noctilucent clouds (Ostdiek and Thomas, 1993; Lange et al., 2022). While it is formally based on human color vision, we used the Mastcam color bands such that the color transform for each pixel was $\{r,g,b\}=\{R,G,B\}/(R+G+B)$, where *RGB* represents *I/F* values for the red, green, and blue channels, and *rgb* represents the normalized color.

2.2 Iridescence and Coronae

We report the first images of nacreous clouds on Mars and of Martian scattering coronae (Fig. 1). Images show clouds that were both noctilucent and iridescent, which are referred to as nacreous clouds on Earth (Ugolnikov et al., 2021). As used here, the terms noctilucent (night-shining), iridescent (colorful due to diffraction), and nacreous (both) refer to the physical and geometric conditions and not to the composition or altitude of analogous terrestrial clouds. For the five mosaics in Fig. 1, each image shows a linear stretch of *I*/*F* that preserves color, enhancing highlights relative to true color. Based on experience imaging terrestrial iridescent clouds, we estimate that the color variations in these clouds would have been visually detectable.

Noctilucent clouds were seen on sol 2422 (L_S=33°) and were widespread on sol 2425 (L_S=34°) but were not abundant after that during the first season (MY-35). The sol-2425 images near the sunset azimuth provided the first evidence for iridescence, and low-scattering-angle images showed the first corona.

Color imaging was initiated earlier in the second season (MY-36). Over several weeks, widespread iridescent clouds and some coronae were seen. On sol 3063 (L_S=19°), the rover was kept awake for several hours from before sunset until dark as a large set of imaging was done under cloudy skies. Clouds became rarer later in the season.

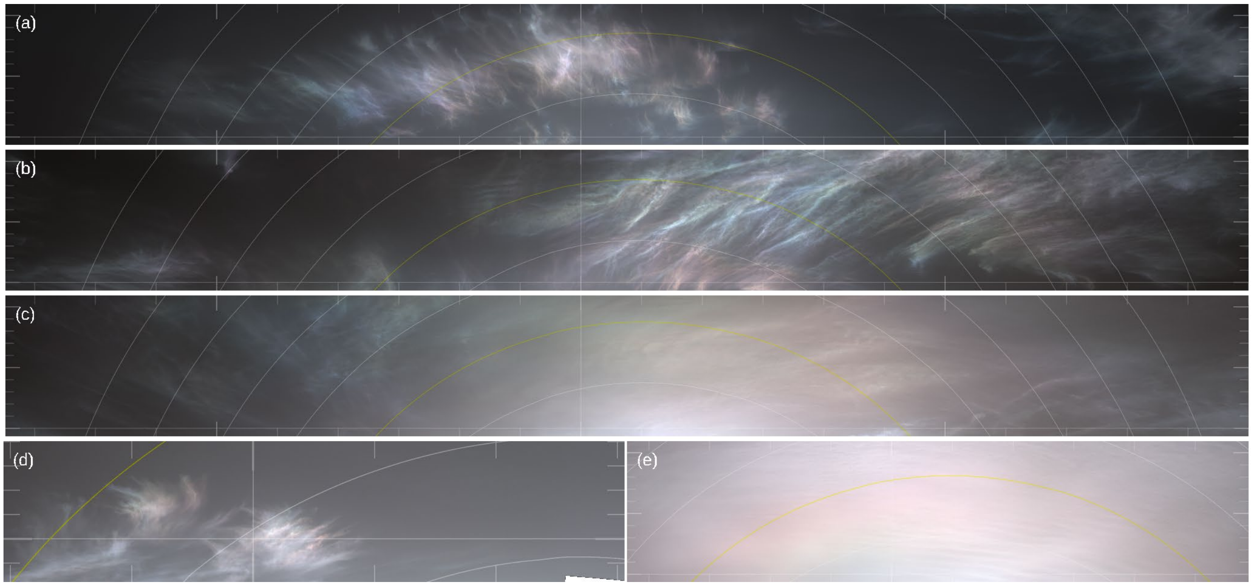

Figure 1: Iridescent clouds are shown in cylindrical projection. Mosaics are shown from sols (a) 3047, (b) 3048, (c) 3050, (d) 2425, and (e) 3049. The axes are at azimuth 270°, elevation 15°, with tick marks every 5° (azimuth) and 1° (elevation). Scattering-angle contours are at 5° intervals with a yellow 30° contour. The image in (d) is shown at twice the resolution of the others.

Iridescence in clouds is a diffraction phenomenon (Sassen, 2003). Locally (e.g., within a few pixels), particle sizes have low variance. Diffraction variations at similar scattering angles indicate a changing size parameter ($\alpha=2\pi a/\lambda$, where a is the particle radius and λ is the wavelength of light). A large local particle-size variance would eliminate iridescence due to the overlap of different-sized diffraction patterns. The low variance suggests that the particles have a similar and short formation history without time to diverge.

A corona in clouds (Fig. 1e) is a diffraction phenomenon with low variance in particle size locally and over large areas of the sky (Lock & Yang, 1991). Color variations appear due to the different widths of the diffraction rings with different wavelengths. Where iridescence indicates that particles locally have the same formation, coronae indicate that a widespread haze has a similar formation history.

3 Environmental Context

3.1 Ultraviolet Photometry

The seasonality of the clouds is important for aiding inferences about their properties and as a tool for planning further studies. While imaging in MY-35 showed evening twilight clouds appeared over L_S=16-33°, no image-based constraints existed before MY-35.

The Rover Environmental Monitoring Station (REMS; Gómez-Elvira et al., 2012) includes an Ultraviolet Sensor (UVS; Smith et al., 2016; Vicente-Retortillo et al., 2017). REMS has typically monitored the first 5 minutes of each hour (in local mean solar time) and several complete hours each sol on a rotating basis. UVS has six photodiode-based sensors covering different spectral ranges with an FOV ±30° from the rover's zenith. The ABC and A sensors, 200-380 nm and 320-380 nm, have the greatest response to twilight due to the combination of bandwidth and available solar flux. Digitized UVS data are truncated at 0 on the rover, making all negative measurements indistinguishable. The A and C (200-280 nm) sensors have the highest 0-points and are thus most useful for low-light studies as they do not saturate low as easily. We use partly calibrated data, showing the current from each photodiode (TELRDR dataset) instead of the fully corrected data with unwanted spatial corrections based on the assumption the light source is direct sunlight. For the brighter clouds, all UVS channels responded the same way; we chose to use channel A as a reference for its combination of response and zero point. Data were taken at 1 Hz; we used 60-s averages (roughly averaging over 0.25° in solar elevation).

We determined that the UVS was sensitive to the clouds present during the imaged period and had recorded cloud-related signals before MY-35. As an initial screen, we averaged the UV-A current when the Sun was 5.5-6.5° down. Figure 2a shows this UV-A current across seasons, demonstrating that there are systematically higher (and variable) signals in the L_S=0-45° period compared to surrounding periods, as well as sporadic high signals near mid-year and a longer period of elevated signals in the second half of the year.

Inspection of the UV-A profile on all nights with appropriate measurements showed a seasonal pattern. For L_S=0-45°, most nights showed a falling signal due to sunset, then a pause or even reversal (see Fig. 2b) followed by a brightness peak. This was also true for some of the sporadic high signals. For most nights from L_S=150-300°, any high signals were consistent with dust extending to higher altitudes at this time of year. Figure 2b shows an example from each Mars year of a signal with a post-sunset peak as well as two out-of-season examples and a dusty season example.

We infer that the sols with a brightness maximum after sunset generally show cloud formation. A uniform spherical shell would have a monotonically decreasing brightness as the Sun lowered. Clouds could advect into or out of the FOV to cause brightness variations. However, if advection were the explanation, clouds would be equally likely to enter or leave the FOV just before the Sun got to -6°. No sudden, early darkening was observed over the L_S=0-45° timeframe. On the other hand, clouds that form at or after sunset should lead to brightening for as long as they are illuminated, followed by darkening based on when the Sun is obscured at their altitude.

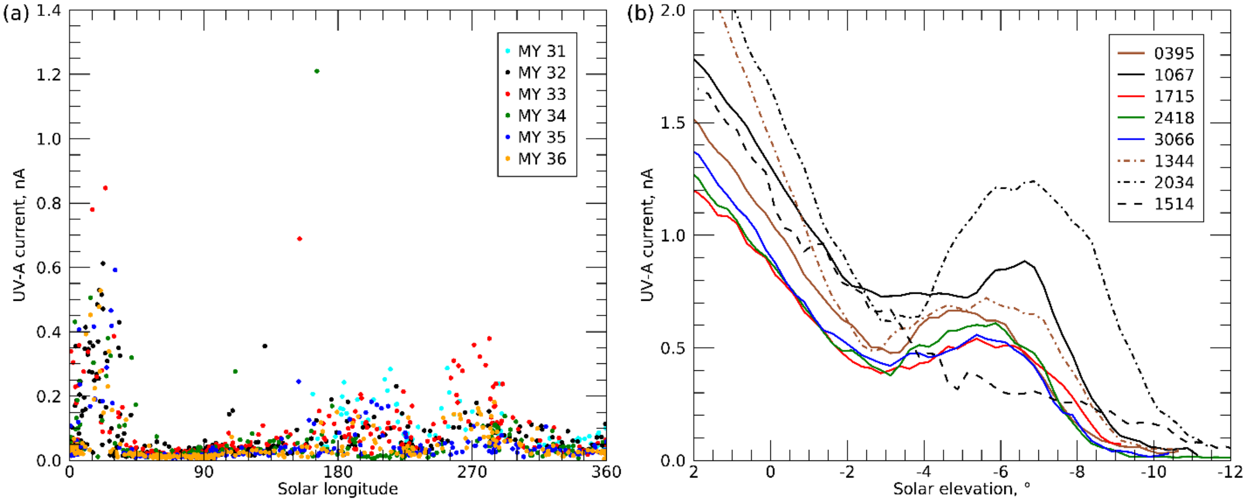

Figure 2: REMS-UVS current indicates clouds. (a) The UVS signal at a solar depression angle of 6° is shown across solar longitudes showing a cloudy season for L_S<45°. Elevated values for L_S>150° mostly correspond to high-altitude dust. (b) UVS profiles for five nights in the noctilucent cloud season are shown with solid lines, two nights with unseasonal noctilucent clouds are shown with dash-dot lines, and a representative dusty season night is shown with a dashed line. One degree corresponds to ~4 minutes.

3.2 Navcam Images and Image Processing

The rover's navigation camera, Navcam, was used as a cloud survey camera due to its wide FOV. Navcam takes monochrome (600-800 nm bandpass) images with a 45° FOV and 1024×1024 detector (Maki et al., 2012). Initial surveys were multi-frame time-lapse images in a single direction, frequently 8 images looking northward toward InSight's location (1×1×8). Other surveys included 3×1 panoramas that were repeated some number of times (3×1×N), and there was occasional use of larger panoramas. Mean-frame subtraction techniques used for daytime images (Moores et al., 2015) were unnecessary for these high-contrast clouds. The cloud contrast was such that autoexposure was an efficient cloud detector: it resulted in short exposures of 1-10 s in the presence of clouds and long exposures of up to 4-5 minutes on cloud-free nights (cf., typical daytime exposures near 0.5 s). As sequence execution windows were based on rapid imaging, the sequences did not run to completion on cloud-free nights.

Imaging campaigns were initiated with Navcam on sols 2400 (L_S=22°) and 3046 (L_S=11°). The initial goals were to confirm that Curiosity's position allowed images of the clouds previously seen by InSight looking to the south (Banfield et al., 2020) and then to further characterize them. With iridescence that could only be observed with Mastcam, the role of

Navcam shifted to providing contextual information. The 3×1×N image sequences were chosen as a standard that could show both low-scattering angle bright sky and high-scattering angle sky that might include the projection of the terminator on clouds. As with Mastcam, geometric information in the image headers was used to create cylindrical mosaics.

3.3 Cloud Morphology, Altitude, and Optical Depth

Shadows cast upward onto the clouds were the most direct clues to altitude in the imaging or UVS photometry. Within the UVS profiles, the rapid brightness fall-off at low solar elevations was interpreted to be caused by the setting of the Sun as seen from the cloud altitude, 30-40 minutes after sunset. In time-lapse images, clouds could be seen going dark over time. In some cases (with appropriate contrast settings), a terminator-like line could be seen across the sky.

We modeled noctilucent cloud brightness as singly scattered sunlight. For a grid of cloud altitudes (arbitrarily using 1-km cloud thickness), solar zenith angles, and atmospheric optical depths, we constructed look-up tables of cloud illumination. We estimated transmission to the cloud layer, scattering by the cloud, and transmission to the rover using measured atmospheric optical depths (Lemmon et al., 2024). We used the look-up tables to associate altitudes with UVS profiles and images with the terminator (see Supporting Information Text S1 for more detail). For Mastcam images, we determined path optical depths through selected locations in clouds using the computed transmissions, the I/F difference between the cloud and the background, and the radiative transfer equation for single scattering. Typical optical depths for the iridescent clouds were 10^{-3} to 10^{-2}.

Figure 3 shows a set of Navcam mosaics with candidate terminators superposed on the images and the resulting height measurements. We assigned a height measurement in a set of images if clouds could be seen to vanish over time (to differentiate changing illumination from patterns in the clouds). We assigned a lower limit to individual images or to a set of images that did not meet that criterion if noctilucent clouds were present. We note that in Fig. 3a, there are both waveform and cirriform clouds (cf., Supporting Information Movie S1). The waves disappear at 50-55 km, while the cirriform clouds disappear at 60-65 km. We chose the cirriform value for the summary in Fig. 3b, but note that sols 3054, 3063, 3075, and 3081 had waveform clouds near 50 km. Clouds moved east-to-west on all nights when motion could be determined.

We tested all sols with >600 s of UVS data while the Sun was 4 to 8° below the horizon. We identified 131 profiles during L_S=0-45°: 84 had no identified clouds and 47 had clouds for which we determined a height (36%); 30 of those had a brightness reversal. We identified 802 profiles during L_S=45-360°, of which 14 gave a height (1.7%) and 6 had a brightness reversal. This reinforces that L_S=0-45° is a distinct cloud season.

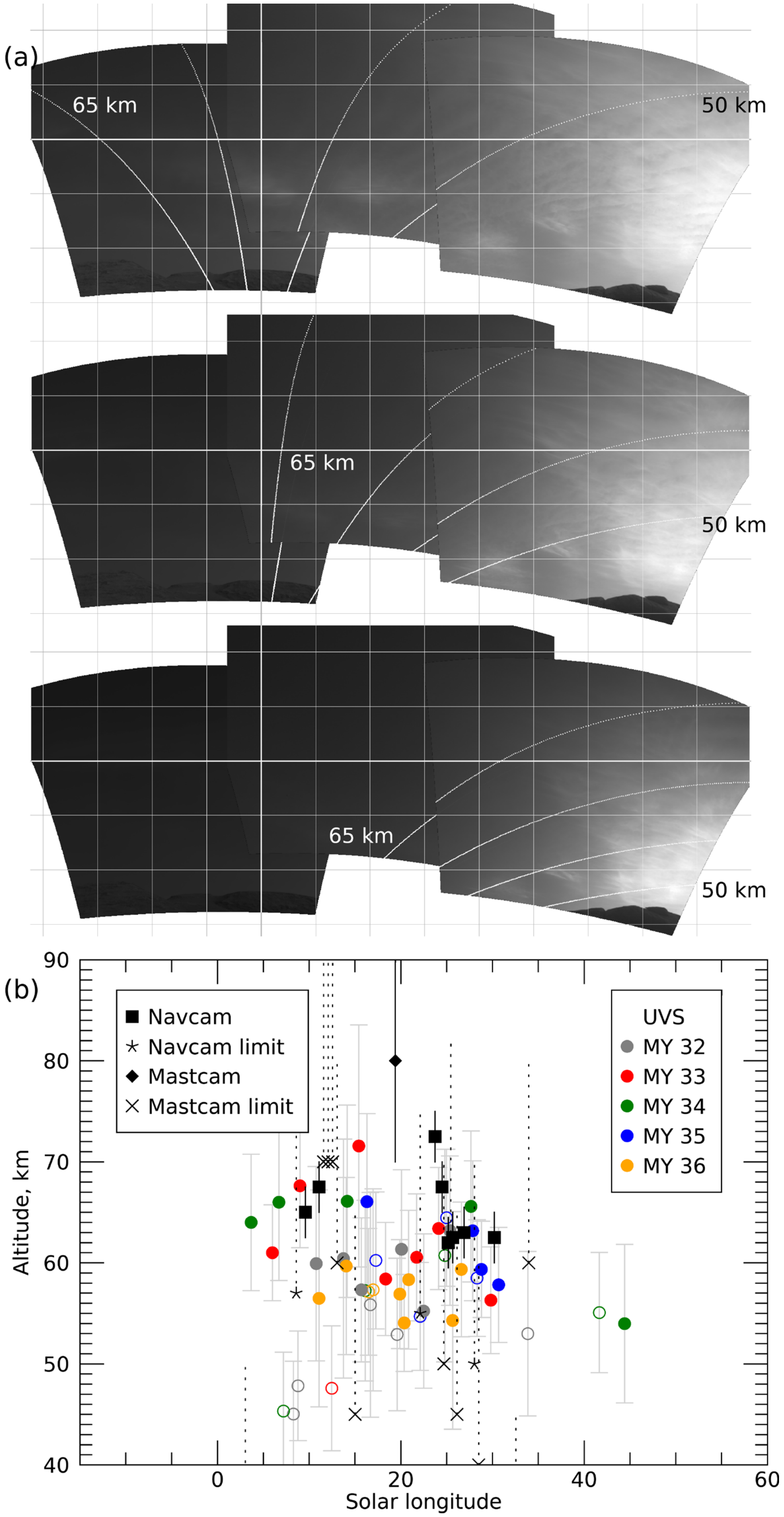(a)
65 km
50 km
65 km
50 km
65 km
50 km
(b)
Navcam
Navcam limit
Mastcam
Mastcam limit
UVS
MY 32
MY 33
MY 34
MY 35
MY 36
Altitude, km
90
80
70
60
50
40
0
20
40
60
Solar longitude

Figure 3: Cloud altitudes are estimates from UV signals and images. (a) Three Navcam twilight mosaics taken over 7.5 minutes on sol 3075 are shown in cylindrical projection with white contours indicating the position of the terminator for cloud altitudes of 50, 55, 60, and 65 km and 10° grid spacing. (b) Cloud altitudes derived from REMS, Navcam, and Mastcam are shown. For REMS-UVS, filled circles indicate nights with brightness reversals, and open circles indicate nights without. For the cameras, filled symbols indicate heights measured in time-lapse imaging, and * and × indicate lower limits from single images.

---

4 Results and Discussion

4.1 Cloud Characteristics

These images include at least two cloud populations: common cirriform clouds and occasional waveform clouds. We do not exclude clouds below 40 km, but due to the detection method, we focus on those above 40 km. Due to the low cloud optical depths, images show a superposition of illuminated clouds. Coronae may be associated with the waveform clouds.

Cirriform clouds at 55-80 km were likely CO_2 ice, but H_2O ice cannot be ruled out from altitude alone. Aoki et al. (2018) reported daytime mesospheric clouds of sub-µm CO_2 east of the site for early autumn, while Clancy et al. (2019) found H_2O ice below 55 km and sub-µm CO_2 up to 70 km at L_S=30-60°.

Waveform clouds, some below 55 km, may have been H_2O ice. Such clouds are seen in daylight, mostly with optical depths near 0.01 around the equinox, transitioning to 0.1 in mid-autumn and winter (Kloos et al., 2018; Hayes et al., 2024). However, these clouds are mainly around 20-40 km altitude (Campbell et al., 2020). Cooper et al. (2018) suggested H_2O ice clouds, as opposed to high and cold CO_2 clouds, cause warming of overnight minimum surface temperatures during L_S=20-50°. We note that coronae are common in terrestrial wave clouds due to their tendency to monodisperse particle sizes (Shaw and Neiman, 2003). Projecting the images to the 50-km level, we find mean wavelengths of 7.5 km, with a range of 5.4-10.8 km, and an orientation consistent with mean motion from 80° azimuth (east).

4.2 Cloud particle size and evolution

While size controls the observed diffraction pattern, a unique interpretation of the diffracted light requires identifying the diffraction pattern over some scale. We calculated the single-scattering phase function for diffraction following Laven (2015) for the relevant scattering angles and a range of sizes, using the camera's spectral response and a log-normal size distribution with σ=0.005, and converted them from linear *RGB* color to normalized *rgb* color (Fig 4a). Other than the number of fringes that can be seen, the width of the distribution has little effect on the colors (Reichardt et al., 2015). Large-scale patterns, such as a corona, could indicate size equilibria, while small-scale patterns could indicate nucleation areas or growth in fall streaks (e.g., Sassen, 1979).

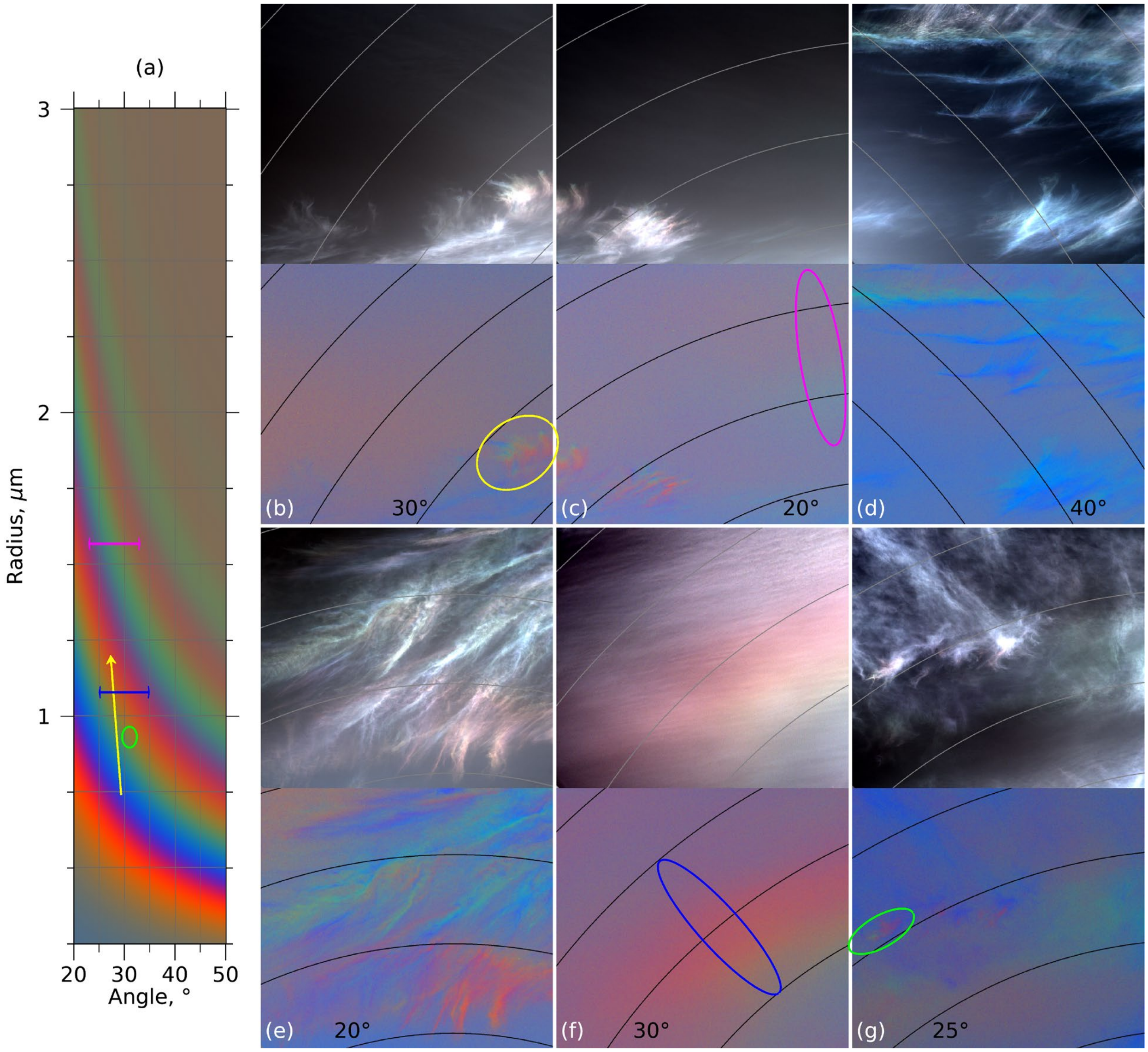

Figure 4: Color constraints on size are shown. (a) Diffraction colors are shown for a narrow log-normal size distribution. Individual M-34 images are shown for sols 2425 (b), 2425 (c), 3047 (d), 3048 (e), 3049 (f), and 3063 (g) with a linear *RGB* stretch above and normalized *rgb* below. Linear stretches are color-neutral from 0.5 to 99.5% brightness levels. The *rgb* stretches are 0.30-0.3667. Contours are every 5° in scattering angle. The yellow ellipse (b) shows color variation in a fall streak represented by the yellow arrow in (a). The magenta ellipse (c) and blue ellipse (f) indicate coronae that correspond to the blue and magenta lines in (a). The green ellipse in (g) shows a region with new small particles.

We looked for a diffraction fingerprint in the clouds, either local color changes at similar scattering angles or larger coronae. Figure 4 shows details (individual images) from several panoramas (also see Supporting Information Figs. S2-S4). Most show iridescent fall streaks, and two show a corona. A fall streak similar to those commonly seen as a result of icy precipitation in terrestrial cirrus clouds in Fig. 4b (and partly 4c) shows a blue-green-red variation. The blue is distinctive in the diffraction calculation and anchors our interpretation that the particles grow from ~0.75 to ~1.2 μm as they fall. However, different assumptions in the diffraction calculation might allow a 1.2 to 1.8 μm interpretation. Options in between are ruled out by the blue, and growth is required by the blue-green-red sequence. Other scenes are more complicated: Fig. 4d shows clouds 40-50° from the Sun, where the relative blueness of ice compared to background dust dominates, but color variations along fall streaks are still present at the top; Fig. 4e shows a set of partially superposed clouds with most of the color variation organized by scattering angle, but some cloud-to-cloud and intracloud variation. The ellipse in Fig. 4f (like 4c) crosses a diffraction fringe in the corona. A single fringe is difficult to interpret given the background light, but examination of several color stretches led to the conclusion that ~1.1 μm was likely, ~0.6 μm less likely, and larger was unlikely. The most intriguing suggestion about cloud physics information that could be teased out of the data was a small color change in the sol-3063 3×2×2 (Fig. 4g). Over 62 s, a greenish area expanded on the left of the red-toned cloud. A possibility is that small particles were actively nucleating in this cloud and became visible at <1 μm.

The linking of size and color through diffraction gives us a window into otherwise hidden cloud formation. While some size interpretations are non-unique, the main conclusion is that there are narrow size distributions, and the colors change with changing size. Kärcher (2022) suggested a possible mechanism: once there are sufficient ice nuclei, further nucleation can be inhibited in favor of uniform depositional growth. The images show evolving clouds, and the colors provide a way to constrain size and growth.

4.3 Open Questions

Additional observations from November 2024 to March 2025 and October to December 2026 could expand the utility of the initial data. (1) How extensive are these clouds, vertically and horizontally? Curiosity and InSight data only pertain to a few hundred km around their landing sites. Orbiters capable of sunset and twilight times could constrain the cloud altitude. (2) How fast do particles evolve in these clouds? Time-lapse imaging, perhaps at a higher resolution, could acquire a significant sample of case studies. (3) What is the nature of the corona-forming layer? The low sample size precludes a convincing association with the waveform clouds, and a larger sample could disambiguate whether the corona is related to the cirriform clouds or if a second process produces a narrow distribution of ice particles. A convincing size for the coronal clouds would require seeing more diffraction rings and, thus, a wider range of angles.

5 Conclusions

The Curiosity rover obtained the first images of iridescence in clouds on Mars and the first detection of a Martian scattering corona. The iridescent clouds were seen in twilight in the early southern autumn of two Mars years, and a five-Mars-year record of ultraviolet photometry shows that this is a consistent and distinctive cloud season. Cirriform clouds at 60-80 km were likely CO_2 clouds, although such clouds were not previously expected. Waveform clouds below 55 km may have been H_2O ice also seen in daytime rover imaging. The diffraction color fringes illustrate size evolution in the clouds, but a larger sample is needed to address timescales for growth and sedimentation.

Acknowledgments

We are grateful to the Curiosity team for their support and the rover time and energy that was allocated to allow for the images that form the basis of this work. The research was conducted partly at the Jet Propulsion Laboratory, California Institute of Technology, under a contract with the National Aeronautics and Space Administration (80NM0018D0004). M.T.L.

was supported via sub-contract 18-1187 from Malin Space Science Systems, Inc. A.V.-R. was funded by the Spanish Ministry of Science and Innovation (MCIN) /State Agency of Research (AEI) project PID2021-126719OB-C41, funded by MCIN/AEI/10.13039/501100011033/FEDER, UE. S.D.G. was supported by the Mars Science Laboratory Participating Scientist program. M.C.M was supported by JPL Contract 1516826 to Malin Space Science Systems.

Open Research

All Curiosity data used in this study are publicly available via the Planetary Data System (Gómez-Elvira, 2013; Malin, 2013; Maki, 2018).

References

Aoki, S., Y. Sato, M. Giuranna, P. Wolkenberg, T.M. Sato, H. Nakagawa, and Y. Kasaba (2018). Mesospheric CO_2 ice clouds on Mars observed by Planetary Fourier Spectrometer onboard Mars Express. *Icarus* **302**, 175-190. DOI: 10.1016/j.icarus.2017.10.047

Atwood, S.A., M.D. Smith, K. Badri, C.S. Edwards, P.R. Christensen, M.J. Wolff, F. Forget, S. Anwar, N. Smith, and M.R. El-Maarry (2022). Diurnal variability in EMIRS daytime observations of water ice clouds during Mars aphelion-season. Geophys. Res. Lett. 49, e2022GL099654. DOI: 10.1029/2022GL099654

Banfield, D., A. Spiga, C. Newman, F. Forget, M. Lemmon, R. Lorenz, N. Murdoch, D. Viudez-Moreiras, J. Pla-Garcia, R. Garcia, P. Lognonné, C. Perrin, L. Martire, Ö. Karatekin, N. Teanby, B. Van Hove, J. Maki, B. Kenda, N. Mueller, S. Rodriguez, T. Kawamura, J. McClean, A. Stott, C. Charalambous, E. Millour, C. Johnson, A. Mittelholz, A. Määttänen, S. Lewis, J. Clinton, S. Stähler, S. Ceylan, D. Giardini, T. Warren, W. Pike, I. Daubar, M. Golombek, L. Rolland, R. Widmer-Schnidrig, D. Mimoun, É. Beucler, A. Jacob, A. Lucas, M. Baker, V. Ansan, K. Hurst, L. Mora-Sotomayor, S. Navarro Lopez, J. Torres, A. Lepinette, A. Molina, M. Marin-Jimenez, J. Gomez-Elvira, V. Peinado, J. Rodriguez-Manfredi, B. Carcich, S. Sackett, C. Russell, T. Spohn, S. Smrekar, and W. Banerdt (2020). The atmosphere of Mars as observed by InSight. *Nature Geoscience*, **13**, 190-198. DOI: 10.1038/s41561-020-0534-0

Bell III, J.F., A. Godber, S. McNair, M.A. Caplinger, J.N. Maki, M.T. Lemmon, J. Van Beek, M.C. Malin, D. Wellington, K.M. Kinch, M.B. Madsen, C. Hardgrove, M.A. Ravine, E. Jensen, D. Harker, R.B. Anderson, K.E. Herkenhoff, R.V. Morris and E. Cisneros. The Mars Science Laboratory Curiosity Rover Mast Camera (Mastcam) Instruments: Pre-Flight and In-Flight Calibration, Validation, and Data Archiving (2017). *Earth and Space Science* **4**, 396-452. DOI: 10.1002/2016EA000219.

Campbell. C., S. Guzewich, C. Smith, J. Kloos, M. Lemmon, C.A. Moore, B. Cooper, R. Haberle, and J. Moores (2020). Estimating the Altitudes of Martian Water-Ice Clouds Above the Mars Science Laboratory Rover Landing Site. *Planet. Space Sci.,* **182**, 104785. DOI: 10.1016/j.pss.2019.104785

Clancy, R.T., M.J. Wolff, M.D. Smith, A. Kleinböhl, B.A. Cantor, S.L. Murchie, A.D. Toigo, K. Seelos, F. Lefèvre, F. Montmessin, F. Daerden, B.J. Sandor (2019). The distribution, composition, and particle properties of Mars mesospheric aerosols: An analysis of CRISM visible/near-IR limb spectra with context from near-coincident MCS and MARCI observations. Icarus 328, 246-273. DOI: 10.1016/j.icarus.2019.03.025

Connour, K., N. M. Schneider, Z. Milby, F. Forget, M. Alhosani, A. Spiga, E. Millour, F. Lefèvre, J. Deighan, S.K. Jain, and M.J.Wolff (2020). Mars's Twilight Cloud Band: A New Cloud Feature Seen During the Mars Year 34 Global Dust Storm. Geophys. Res. Lett. 47, e2019GL084997. DOI: 10.1029/2019GL084997

Cooper, B., M. de la Torre Juarez, M. Mischna, M. Lemmon, G. Martinez, D. Kass, A.R. Vasavada, C. Campbell, and J. Moores, 2021. Thermal forcing of the nocturnal near surface environment by Martian water ice clouds. *J. Geophys. Res*. **126**, e2020JE006737. DOI: 10.1029/2020JE006737.

[dataset] Gomez-Elvira, J. (2013). Mars Science Laboratory Rover Environmental Monitoring Station RDR Data V1.0, MSLREM_1001, NASA Planetary Data System. https://pds-atmospheres.nmsu.edu/cgi-bin/getdir.pl?volume=mslrem_1001

Gómez-Elvira, J., C. Armiens, L. Castañer, M. Domínguez, M. Genzer, F. Gómez, R. Haberle, A.-M. Harri, V. Jiménez, H. Kahanpää, L. Kowalski, A. Lepinette,J. Martín, J. Martínez-Frías, I. McEwan, L. Mora, J. Moreno, S. Navarro,M.A. de Pablo, V. Peinado, A. Peña, J. Polkko, M. Ramos, N.O. Renno, J. Ricart,M. Richardson, J. Rodríguez-Manfredi, J. Romeral, E. Sebastián, J. Serrano,M. de la Torre Juárez, J. Torres, F. Torrero, R. Urquí, L. Vázquez, T. Velasco,J. Verdasca, M.-P. Zorzano, J. Martín-Torres (2012). REMS: The Environmental Sensor Suite for the Mars Science Laboratory Rover. *Space Sci. Rev.* **170**, 583–640. DOI 10.1007/s11214-012-9921-1

Hayes, C.W., J.L. Kloos, A.C. Innanen, C.L. Campbell, H.M. Sapers, and J.E. Moores (2024). Five Mars Years of cloud observations at Gale Crater: Opacities, variability, and ice crystal habits. *Plan. Sci. J.* **5**, 51. DOI: 10.3847/PSJ/ad2202

Hernández-Bernal, J., Sánchez-Lavega, A., del Río-Gaztelurrutia, T., Hueso, R., Ravanis, E., Cardesín-Moinelo, A., S. Wood, and D. Titov (2021). A long-term study of Mars mesospheric clouds seen at twilight based on Mars Express VMC images. *Geophys. Res. Lett.*, **48**, e2020GL092188. DOI: 10.1029/2020GL092188

Jiang, F. Y., R.V. Yelle, S.K. Jain, J. Cui., F. Montmessin, N.M. Schneider, J. Deighan, H. Gröller, and L. Verdier (2019). Detection of mesospheric CO_2 ice clouds on Mars in southern summer. *Geophysical Research Letters*, **46**, 7962–7971. DOI: 10.1029/2019GL082029

Kärcher, B. (2022). A parameterization of cirrus cloud formation: Revisiting competing ice nucleation. *J. Geophys. Res*., **127**, e2022JD036907. DOI: 10.1029/2022JD036907

Kloos, J.L., J.E. Moores, J.A. Whiteway, and M. Aggarwal (2018). Interannual and Diurnal Variability in Water Ice Clouds Observed from MSL Over Two Martian Years. *J. Geophys. Res.* **123**, 233–245. DOI: 10.1002/2017JE005314

Lange, A., G. Baumgarten, A. Rozanov, and C. von Savigny (2022). On the colour of noctilucent clouds. *Ann. Geophys*. **40**, 407-419. DOI: 10.5194/angeo-40-407-2022

Laven, P. (2015). Re-visiting the atmospheric corona. *Appl. Opt*. **54**, B46-B53. DOI: 10.1364/AO.54.000B46.

Lemmon, M.T., M.J. Wolff, J.F. Bell III, M.D. Smith, B. Cantor, and P.H. Smith (2015). Dust aerosol, clouds, and the atmospheric optical depth record over 5 Mars years of the Mars Exploration Rover mission. *Icarus* **251**, 96-111. DOI: 10.1016/j.icarus.2014.03.029.

Lemmon, M.T., J.F. Bell III, and A.G. Hayes (2022). Revised Radiative Response Coefficients for the Curiosity Rover Mastcam from Direct Solar Images and Analog Tests. Res. Notes AAS 7, 29. DOI 10.3847/2515-5172/acbc11.

Lemmon, M.T., S.D. Guzewich, J.M. Battalio, M.C. Malin, A. Vicente-Retortillo, M.-P. Zorzano, J. Martín-Torres, R. Sullivan, J.N. Maki, M.D. Smith, J.F. Bell III (2024). The Mars Science Laboratory record of optical depth measurements via solar imaging. *Icarus*, **408**, 115821. DOI: 10.1016/j.icarus.2023.115821

Liuzzi, G., G.L. Villanueva, L. Trompet, M.M.J. Crismani, A. Piccialli, S. Aoki, M. A. Lopez-Valverde, A. Stolzenbach, F. Daerden, L. Neary, M. D. Smith, M.R. Patel, S. R. Lewis, R. T. Clancy, I. R. Thomas, B. Ristic, G. Bellucci, J.-J. Lopez-Moreno, and A. C. Vandaele (2021). First detection and thermal characterization of terminator CO2 ice clouds with ExoMars/ NOMAD. *Geophys. Res. Lett.*, **48**, e2021GL095895. DOI: 10.1029/2021GL095895

Lock, J.A., and L. Yang (1991). Mie theory of the corona. *Appl. Opt*. **30**, 3408–3414.

Määttänen, A., F. Montmessin, B. Gondet, F. Scholten, H. Hoffmann, F. González-Galindo, A. Spiga, F. Forget, E. Hauber, G. Neukum, J.-P. Bibring, J.-L. Bertaux (2010). Mapping the mesospheric CO2 clouds on Mars: MEx/OMEGA and MEx/HRSC observations and challenges for atmospheric models. *Icarus* **209**, 452-469. DOI: 10.1016/j.icarus.2010.05.017

[dataset] Maki, J. (2018). MSL Mars navigation camera 5 RDR V2.0 [Dataset]. NASA Planetary Data System. DOI: 10.17189/1519572

Maki, J., D. Thiessen, A. Pourangi, P. Kobzeff, T. Litwin, L. Scherr, S. Elliott, A. Dingizian, and M. Mamone (2012). The Mars Scienec Laboratory engineering cameras. Space Sci. Rev. 170, 77-93. DOI: 10.1007/s11214-012-9882-4

[dataset] Malin, M., MSL Mars Mast Camera EDR V1.0, NASA Planetary Data System, MSL-M-MASTCAM-2-EDR-IMG-V1.0, 2013. DOI: 10.17189/1520190.

Malin, M.C., M.A. Ravine, M.A. Caplinger, F.T. Ghaemi, J.A. Schaffner, J.N. Maki, J.F. Bell III, J.F. Cameron, W.E. Dietrich, K.S. Edgett, L.J. Edwards, J.B. Garvin, B. Hallet, K.E. Herkenhoff, E. Heydari, L.C. Kah, M.T. Lemmon, M.E. Minitti, T.S. Olson, T.J. Parker, S.K. Rowland, J. Schieber, R. Sletten, R.J. Sullivan, D.Y. Sumner, R.A. Yingst, B.M. Duston, S. McNair, and E.H. Jensen (2017). The Mars Science Laboratory (MSL) Mast cameras and Descent imager: I. Investigation and instrument descriptions. *Earth and Space Science* **4**, 506-539. DOI: 10.1002/2016EA000252

Montmessin, F., B. Gondet, J.-P. Bibring, Y. Langevin, P. Drossart, F. Forget, and T. Fouchet (2007), Hyperspectral imaging of convective CO2 ice clouds in the equatorial mesosphere of Mars, *J. Geophys. Res*., **112**, E11S90, doi: 10.1029/2007JE002944.

Moores, J., M.T. Lemmon, S.C.R. Rafkin, R. Francis, J. Pla-Garcia, M. de la Torre Juárez, K. Bean*, D. Kass, R. Haberle, C. Newman, M. Mischna, A. Vasavada, N. Rennó, J. Bell, F. Calef, B. Cantor, T.H. Mcconnochie, A.-M. Harri, M. Genzer, M. Wong, M.D. Smith, F.J. Martín-Torres, M.-P. Zorzano, O. Kemppinen, and E. McCullough (2015). Atmospheric movies acquired at the Mars Science Laboratory landing site: Cloud Morphology, Frequency and Significance to the Gale Crater Water Cycle and Phoenix Mission Results. *Adv. Space Res*. **55**, 2217-2239. doi:10.1016/j.asr.2015.02.007.

Ostdiek, V.J., and G.E. Thomas (1993). Visible spectra and chromaticity of noctilucent clouds. *J. Geophys. Res*. **98**, D11, 20347-20356.

Reichardt, J., S. Reichardt, C.A. Hostetler, P.L Lucker, T.J. McGee, L.W. Twigg, A. Dörnbrack, M.R. Schoeberl, and P. Yang (2015). Mother-of-pearl cloud particle size and composition from aircraft-based photography of coloration and lidar measurements. *Appl. Opt.* **54**, B140-B153. DOI: 10.1364/AO.54.00B140

Sánchez-Lavega, H. Chen-Chen , I. Ordoñez-Etxeberria, R. Hueso, T. del Río-Gaztelurrutia, A. Garro, A. Cardesín-Moinelo, D. Titov, S. Wood (2018). Limb clouds and dust on Mars from images obtained by the Visual Monitoring Camera (VMC) onboard Mars Express. Icarus 299, 194-205. DOI: 10.1016/j.icarus.2017.07.026

Sassen, K. (1979). Iridescence in an aircraft contrail. *J. Opt. Soc. Am*. **69**, 1080–1083.

Sassen, K. (2003). Cirrus cloud iridescence: a rare case study. Appl. Opt. 42, 486-491.

Sefton-Nash, E., N.A. Teanby, L. Montabone, P.G.J. Irwin, J. Hurley, S.B. Calcutt (2013). Climatology and first-order composition estimates of mesospheric clouds from Mars Climate Sounder limb spectra. *Icarus* **222**, 342-356. DOI: 10.1016/j.icarus.2012.11.012

Shaw, J.A., and P.J. Neiman (2003). Coronas and iridescence in mountain wave clouds. *Appl. Opt*. **42**, 476-485.

Slipsky, M., A. Kleinböhl, S. Dillmann, D.M. Kass, J. Reimuller, M. Wronkiewicz, G. Doran, 2024. The Cloudspotting on Mars citizen science project: Seasonal and spatial cloud distributions observed by the Mars Climate Sounder. *Icarus*, **419**, 115777. DOI: 10.1016/j.icarus.2023.115777.

Smith, M.D., M.J. Wolff, R.T. Clancy, A. Kleinböhl, and S.L. Murchie (2013). Vertical distribution of dust and water ice aerosols from CRISM limb-geometry observations, *J. Geophys. Res.*, **118**, 321–334, doi:10.1002/jgre.20047

Smith, M.D., M-P. Zorzano, M. Lemmon, J. Martin-Torres, and T. Mendaza de Cal (2016). Aerosol optical depth as observed by the Mars Science Laboratory REMS UV photodiodes. *Icarus* **280**, 234-248. doi: 10.1016/j.icarus.2016.07.012.

Smith, P.H., J.F. Bell III, N.T. Bridges, D.T. Britt, L. Gaddis, R. Greeley, H.U. Keller, K.E. Herkenhoff, R. Jaumann, J.R. Johnson, R.L. Kirk, M. Lemmon, J.N. Maki, M.C. Malin, S.L. Murchie, J. Oberst, T.J. Parker, R.J. Reid, R. Sablotny, L.A. Soderblom, C. Stoker, R. Sullivan, N. Thomas, M.G. Tomasko, W. Ward, E. Wegryn, 1997. Results from the Mars Pathfinder Camera. *Science* **278** 1758-1765. doi: 10.1126/science.278.5344.1758.

Spiga, A., F. González-Galindo, M.-Á. López-Valverde, and F. Forget (2012). Gravity waves, cold pockets and CO2 clouds in the Martian mesosphere. *Geophys. Res. Lett*. **39**, L02201. DOI: 10.1029/2011GL050343

Stevens, M. H., D. E. Siskind, J. S. Evans, S. K. Jain, N. M. Schneider, J. Deighan, A. I. F. Stewart, M. Crismani, A. Stiepen, M. S. Chaffin, W. E. McClintock, G. M. Holsclaw, F. Lefèvre, D. Y. Lo, J. T. Clarke, F. Montmessin, and B. M. Jakosky (2017), Martian mesospheric cloud observations by IUVS on MAVEN: Thermal tides coupled to the upper atmosphere, *Geophys. Res. Lett*., **44**, doi:10.1002/2017GL072717.

Szantai, A., J. Audouard, F. Forget, K.S. Olsen, B. Gondet, E. Millour, J.-B. Madeleine, A. Pottier, Y. Langevin, J.-P. Bibring (2021). Martian cloud climatology and life cycle extracted from Mars Express OMEGA spectral images. *Icarus* **353**, 114101. DOI: 10.1016/j.icarus.2020.114101

Toledo, D., L. Gómez-Martín, V. Apéstigue, I. Arruego, M.D. Smith, A. Munguira, G. Martinez, P. Patel, A. Sánchez-Lavega, M.T. Lemmon, L. Tamppari, D. Viúdez-Moreiras, R. Hueso, A. Vicente-Retortillo, C. Newman, R.D. Lorenz, M. Yela, M. de la Torre Juárez, J.A. Rodriguez-Manfredi (2023). Twilight mesospheric clouds in Jezero as observed by MEDA Radiation and Dust Sensor (RDS). *J. Geophys. Res*. **128**, e2023JE007785. http://dx.doi.org/10.1029/2023JE007785.

Ugolnikov, O.S., B.V. Kozelov, S.V. Pilgaev, and A.V. Roldugin (2021). Retrieval of particle size distribution of polar stratospheric clouds based on wide-angle color and polarization analysis. Planet. Space. Sci. 200, 105213. DOI: /10.1016/j.pss.2021.105213

Vicente-Retortillo, Á., G. Martínez, N. Rennó, M.T. Lemmon, M. de la Torre Juarez. Determination of dust aerosol particle size at Gale Crater using REMS UVS and Mastcam measurements (2017). *Geophys. Res. L.*, **44**. doi: 10.1002/2017GL072589.

Vincendon, M., C. Pilorget, B. Gondet, S. Murchie, and J.-P. Bibring (2011), New near-IR observations of mesospheric CO_2 and H_2O clouds on Mars, *J. Geophys. Res.*, **116**, E00J02, doi: 10.1029/2011JE003827.

Wolff, M.J., R.T. Clancy, M.A Kahre, R.M. Haberle, F. Forget, B.A. Cantor, and M.C. Malin (2019). Mapping water ice clouds on Mars with MRO/MARCI. *Icarus* **332**, 24-49. DOI: 10.1016/j.icarus.2019.05.041.